

# Comparison of optical and structural properties of nanostructure TiO<sub>2</sub> thin film doped by Sn and Nb

Behzad Koozegar Kaleji

Received: 4 May 2013 / Accepted: 28 May 2013 / Published online: 4 June 2013  
© Springer Science+Business Media New York 2013

**Abstract** The thin films of TiO<sub>2</sub> doped by Sn or Nb were prepared by sol–gel method under process control. The effects of Sn and Nb doping on the structural, optical and photo-catalytic properties of applied thin films have been studied by X-ray diffraction (XRD) high resolution transmission electron microscopy and UV–Vis absorption spectroscopy. Surface chemical state of thin films was examined by atomic X-ray photoelectron spectroscopy. XRD results suggest that adding impurities has a great effect on the crystallinity and particle size of TiO<sub>2</sub>. Titania rutile phase formation in thin film was promoted by Sn<sup>4+</sup> addition but was inhibited by Nb<sup>5+</sup> doping. The activity of the photocatalyst was evaluated by photocatalytic degradation kinetics of aqueous methylene blue under UV and Visible radiation. The results show that the photocatalytic activity of the Sn-doped TiO<sub>2</sub> thin film have a larger degradation efficiency than Nb-doped TiO<sub>2</sub> under visible light, but under UV light photocatalytic activity of the Nb-doped TiO<sub>2</sub> thin film is better.

**Keywords** Titania thin film · Sol–gel dip coating · Photocatalytic activity · Sn dopant · Nb dopant

## 1 Introduction

Titanium oxide is a well-known photocatalyst working in the ultraviolet (UV) region of light with a band gap of 3.2 eV. Numerous reports are available regarding the shifting of wavelength corresponding to the onset of

absorption from UV to visible region of light in TiO<sub>2</sub> as a consequence of doping it with cationic or anionic dopants. Anionic dopants such as nitrogen, sulphur, carbon and fluorine lead to a narrowing of the band gap of TiO<sub>2</sub>. This results in visible light absorption and improved photocatalytic activity [1–3].

TiO<sub>2</sub> doped with Ce, V, Cu, Sn, Nd, Fe, Cr or Co shows a red shift of the absorption band compared to pure TiO<sub>2</sub>, and considerable photocatalytic activity under visible light irradiation [4–10].

Sensitization of Cu doped TiO<sub>2</sub> with eosin improved the photocatalytic activity for water splitting under visible light irradiation [6]. In this case, CuO not only brings about the charge separation but also provides active sites for water splitting. Doping of TiO<sub>2</sub> with 0.1 % Nd and impregnation with Pt produced enhanced photocatalytic activity for water splitting due to the prevention of phase transformation of TiO<sub>2</sub> from anatase to rutile and inhibition of particle growth [11].

Some recent studies have revealed that the oxygen deficient sites play a crucial role in the visible light induced photocatalytic activity of TiO<sub>2</sub>. Ihara et al. [12] have reported that the low temperature H<sub>2</sub> plasma treated TiO<sub>2</sub> and nitrogen doped TiO<sub>2</sub> [13] showed visible light photocatalytic activity due to the presence of oxygen deficient sites.

Prokes et al. [14] have proposed that the visible light absorption of titanium oxynitride is due to the oxygen hole centre created during the surface modification process by nitrogen near the surface of the nano colloid. The visible light photocatalytic activity observed due to the oxygen vacancies in TiO<sub>2</sub> is found to decrease after an optimum value.

From 1990s, the modification of TiO<sub>2</sub> by metal ions has become a hot topic, and the effect of metal (such as Cu, Fe,

B. Koozegar Kaleji (✉)  
Department of Materials Engineering, Faculty of Engineering,  
Malayer University, P.O. Box:65719-95863, Malayer, Iran  
e-mail: bkaleji@yahoo.com; b.kaleji@malayeru.ac.ir

Ag, Au, Pt, W, V, Pb, Cr, Rh, Co and Ni) ions doping on photocatalytic activity of TiO<sub>2</sub> has been studied widely [15–18]. However, there were some contradictory reports on the activity of TiO<sub>2</sub> modified by metal ions. For example, Chot et al. [18] considered that the activity of TiO<sub>2</sub> could be improved by Fe<sup>3+</sup> doping, but Brezova et al. [19] and Navio et al. [20] revealed that Fe<sup>3+</sup> was harmful to the activity of TiO<sub>2</sub>.

In our previous research, we studied the effect of doping Sn (up to 30 mol%) and Nb (up to 20 mol%) on photocatalytic behavior of titania based thin films. We found that 15 mol% of Sn and 1 mol% on Nb shows the most significant improvement on photo-catalytic behavior of TiO<sub>2</sub> under UV irradiation [21, 22].

In this paper, the thin films of TiO<sub>2</sub>, doped by Sn and Nb, were prepared by sol–gel method. The thin films were applied by sol–gel dip-coating process. The effect of the dopant cations on the structure and optical properties was studied in a systematic way. The efficiency of these samples as photocatalysis for the degradation of MB, as organic compound model, under UV and Visible light, was investigated.

## 2 Experimental procedures

### 2.1 Preparation of the thin films

The preparation of precursor solution for Sn and Nb doped TiO<sub>2</sub> thin films is described as follows: TiO<sub>2</sub>, SnO<sub>2</sub> and Nb<sub>2</sub>O<sub>5</sub> sols were prepared, separately. For the preparation of TiO<sub>2</sub> sol, titanium (IV) butoxide (TBT = Ti(OC<sub>4</sub>H<sub>9</sub>)<sub>4</sub>, Aldrich) was selected as titanium source. First, 0.35 mol ethanol (EtOH, Merck) and 0.04 mol ethyl acetoacetate (EAcAc is as a sol stabilizer during preparation of sol and also chelating agent during coating, Merck) were mixed, and then 0.01 mol TBT was added by the rate of 1 ml/min to the mixture at the ambient temperature (25 °C). The solution was continuously stirred for 45 min, followed by the dropping of HNO<sub>3</sub> as catalyst to the solution until pH of 3. De-ionized water was added to the solution slowly to initiate hydrolysis process. Solution was aged for 24 h in order to complete all reactions. The chemical composition of the resultant alkoxide solution was TBT:H<sub>2</sub>O:HNO<sub>3</sub>:EAcAc:EtOH = 1:10:1:4:35 in molar ratio. In order to prepare SnO<sub>2</sub> sol and Nb<sub>2</sub>O<sub>5</sub> sol, stannous chloride (SnCl<sub>2</sub>·2H<sub>2</sub>O, Merck) and niobium chloride (NbCl<sub>5</sub>, Merck) were dissolved in EtOH with molar ratio of SnCl<sub>2</sub>·2H<sub>2</sub>O:EtOH = 1:35 and NbCl<sub>5</sub>:EtOH = 2:35 at ambient temperature with continuous stirring. Solutions were aged for 24 h in order to complete all reactions. Then, mixtures of TiO<sub>2</sub>, SnO<sub>2</sub>, and Nb<sub>2</sub>O<sub>5</sub> were made with different mol ratios of Sn and Nb (Ti-15 % Sn and T-1 % Nb) at the ambient

temperature. The Sn-doped and Nb-doped TiO<sub>2</sub> thin films were applied on the glazed porcelain substrates with the prepared sol solutions by dipping-withdrawing at room temperature with withdrawal speed of 10 mm/min.

The porcelain substrate composition was Al<sub>2</sub>O<sub>3</sub>:45.12, SiO<sub>2</sub>:43.83, BaO:6.18, K<sub>2</sub>O:3.63, Na<sub>2</sub>O:0.58, MgO:0.39, CaO:0.27 wt%. Glazed composition contained SiO<sub>2</sub>:64.45, Al<sub>2</sub>O<sub>3</sub>:16.56, CaO:6.07, K<sub>2</sub>O:5.1 MgO:4.36, Fe<sub>2</sub>O<sub>3</sub>:3.46 wt%. Porcelain and glaze compositions were reported by substrate manufacturer with formal report.

Substrate dimensions were 30 × 15 × 1 mm. The substrates were degreased in ethanol and cleaned in de-ionized water for 15 min and acetone with supersonic wave. The treated substrate samples were dried at 80 °C for 1 h. In order to prevent diffusion of porcelain substrate and glaze elements to final thin film, one interlayer (buffer layer) SiO<sub>2</sub> thin film with withdrawal speed of 10 mm/min was applied. Silica sol contains tetra ethyl orthosilicate (TEOS, Merck): EtOH:H<sub>2</sub>O:HCl with 1:3.8:1:0.01 molar ratios and calcined at 400 °C for 1 h. Samples were dried at 100 °C for 1 h after each coating cycle and finally heated at a rate of 2 °C/min and calcined at 475 °C for 1 h in air atmosphere.

Substrates were coated with one SiO<sub>2</sub> (buffer layer) and two Sn or Nb-doped TiO<sub>2</sub> layers.

### 2.2 Characterization methods

X-ray diffraction (XRD) pattern and phase identification of thin films were recorded using XRD analysis (Philips, MPD-XPRT, λ:Cu Kα = 0.154 nm). The samples were scanned in the 2θ range of 20°–70°. Morphology of the thin films was observed using scanning electron microscopy (SEM, XL30 Series) with an accelerating voltage of 10–15 kV. X-ray photoelectron spectroscopy (XPS) spectra were recorded by a PHI 5000C ESCA spectrometer using Mg Kα radiation (hν = 1253.6 eV). The pressure of the analyzer chamber was maintained at 5 × 10<sup>-8</sup> Pa. Spectra were calibrated with respect to the C1s peak at 284.6 eV.

N<sub>2</sub> adsorption–desorption isotherms were determined in a surface analyzer equipment (BEL Japan Inc., Osaka, Japan) at 77 K. BET surface area and BJH analyses were used to determine the total specific surface area and the pore size distribution.

In order to make TEM foils, the films were removed from the substrates by water flotation. Droplets of the sol–gel material were also deposited on plain (un-coated) copper grids so as to form free-standing films for in situ hot-stage experiments in the TEM. Conventional TEM imaging and electron diffraction analysis was carried out using an EM-2100F-JEOL-Tokyo-Japan with acceleration voltage of 200 kV.

### 2.3 Photo-catalytic activity measurement

The photo-catalytic activity was evaluated by monitoring the degradation of MB solution (5 ppm) under UV and visible illumination. The samples were placed in 20 ml aqueous MB solution and were kept in dark for 2 h. They were then irradiated from top using a UV lamp (Philips 8 W, 360 nm) and visible irradiation. The high pressure mercury vapor lamp (400 W, Osoram) with UV filter has been used as a visible light source (output is 436–546 nm) with 35,000 lumen. Cut off filter was placed in the path of light for complete removal of UV radiation and running water was circulated around the sample container to filter IR radiation and to keep the reaction mixture at room temperature.

The intensity of the MB characteristic band at 660 nm ( $I_{660}$ ) in the obtained UV–Vis spectrum (varian Cary 50 spectrophotometer) was used to determine the concentration of MB in the solution ( $C_t$ ).

The degradation rate of MB, which represents the photo-catalytic efficiency of the films, can be determined by Eq. 1.

$$d(\%) = (C_0 - C_t)/C_0 \times 100 \quad (1)$$

where  $d$  is degradation rate,  $C_t$  is concentration after radiation and  $C_0$  is concentration before radiation [23].

## 3 Results and discussion

### 3.1 X-ray diffraction studies of the thin films

Figure 1 shows the XRD patterns of the films without and with 15 %Sn, 1 %Nb dopant heat treated at 475 °C for 1 h. XRD peak at 25.5° corresponds to characteristic peak of crystal plane (1 0 1) of anatase, at 27.6° corresponds to characteristic peak of crystal plane (1 1 0) of rutile in films. According to the XRD patterns, the pure TiO<sub>2</sub> (T) constituted of pure anatase phase.

All thin films were identified as the mixture polymorphs of anatase (JCPDS: No. 21-1272) and rutile (JCPDS: No. 21-1276), without any impurity phase. In the phase composition, anatase appeared as the main phase, and rutile crystallization was promoted by Sn<sup>4+</sup> doping but was inhibited by Nb<sup>5+</sup> doping. With the addition of Sn 15 % and Nb 1 %, the intensity of the (101) diffraction peak became weaker than that of the pure TiO<sub>2</sub> film, suggesting that the film with Sn or Nb doping experienced lower crystallization. Other doped samples were also anatase or rutile TiO<sub>2</sub> and no signs of metal or oxide phases of tin or niobium were detected. This suggests the incorporation of Sn<sup>4+</sup> and Nb<sup>5+</sup> in TiO<sub>2</sub> lattice [24, 25].

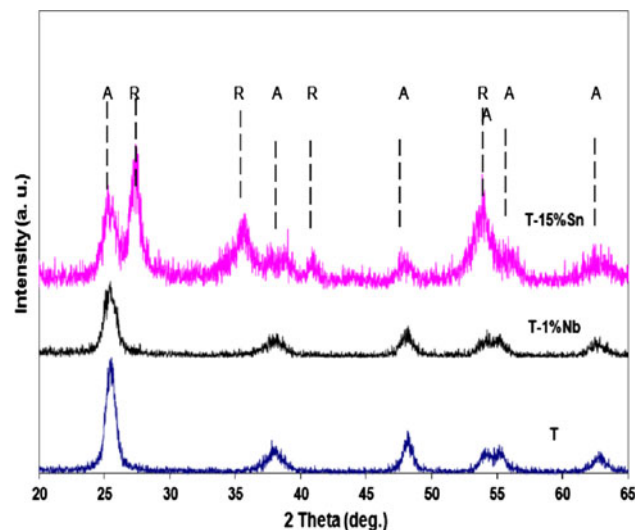


Fig. 1 XRD spectra of the pure and doping TiO<sub>2</sub> films

The diffraction peaks of rutile crystallites appeared in X-ray profiles with increasing Sn dopant in thin films. The addition of Sn has a promoting effect on the transformation of anatase to rutile crystalline phase [26, 27], due to the rutile like structure of SnO<sub>2</sub>-cassiterite phase. It is also found that the peak position of (1 0 1) anatase and (1 1 0) rutile planes shift to a smaller diffraction angle with increasing Sn content in TiO<sub>2</sub> thin films. This may result from the exchange of Ti with Sn in the TiO<sub>2</sub> lattice.

The average crystallite size of thin films ( $D$ ) was determined from the XRD patterns, according to the Scherrer (Eq.2) [28]

$$D = k\lambda/\beta \cos \theta \quad (2)$$

where  $k$  is a constant (shape factor, about 0.9),  $\lambda$  the X-ray wavelength (0.154 nm),  $\beta$  the full width at half maximum (FWHM) of the diffraction peak, and  $\theta$  is the diffraction angle. The values of  $\beta$  and  $\theta$  of anatase and rutile phases were taken from anatase (1 0 1) and rutile (1 1 0) planes diffraction lines, respectively.

The amount of rutile in the samples was calculated using the following equation [29]

$$X_R = (1 + 0.8I_A/I_R)^{-1} \quad (3)$$

where  $X_R$  is the mass fraction of rutile in the samples, and  $I_A$  and  $I_R$  are the X-ray integrated intensities of (1 0 1) reflection of the anatase and (1 1 0) reflection of rutile, respectively. The diffraction peaks of crystal planes (101) (200), and (105) of anatase phase in XRD patterns were selected to determine the lattice parameters of the TiO<sub>2</sub> and doped TiO<sub>2</sub> thin films. The lattice parameters were obtained by using the (Eq.4) [28]

$$(Bragg's\ law) : 2d_{(hkl)} \sin \theta = \lambda$$

$$(1/d_{(hkl)})^2 = (h/a)^2 + (k/b)^2 + (l/c)^2 \tag{4}$$

where  $d_{(hkl)}$  is the distance between the crystal planes of (hkl);  $\lambda$  is the wavelength of X-ray used in the experiment;  $\theta$  is the diffraction angle of the crystal plane (hkl); hkl is the crystal plane index; and  $a$ ,  $b$ , and  $c$  are lattice parameters (in anatase form,  $a = b \neq c$ ).

The characteristic of all thin films after thermal treatment at 475 °C is reported at Table 1. By increasing Sn dopant, transformation of anatase to rutile phase was promoted, the amount of rutile phase structure was increased, and a decrease in the crystalline size was detected. The decrease in crystal size can be attributed to the presence of Sn–O–Ti in the Sn-doped TiO<sub>2</sub> thin films which inhibits the growth of crystal grains [30].

Compared with those of pure TiO<sub>2</sub> films, for doped TiO<sub>2</sub> films, average anatase crystallite sizes decreased. It is found that the Nb dopants can inhibit the anatase grain

**Table 1** The characteristic of dip-coated thin films after thermal treatment at 475 °C

Sample	%A	%R	d <sub>A</sub> (nm)	d <sub>R</sub> (nm)	a = b (Å)	c (Å)	V <sub>u,c</sub> (Å <sup>3</sup> )
T (undoped)	100	–	15.1	–	3.766	9.341	133.162
T-1 %Nb	100	–	12.2	–	3.786	9.347	133.972
T-15 %Sn	36.2	63.8	12.1	14.8	3.809	2.199	31.907

growth. The Nb<sup>5+</sup> radius (0.70 Å) is slightly bigger than Ti<sup>4+</sup> radius (0.64 Å) and this means that Nb<sup>5+</sup> induces slight stress in TiO<sub>2</sub> lattice, which may hinder the growth of the TiO<sub>2</sub> crystallites as was found by Sharma and Bhatnagar [24].

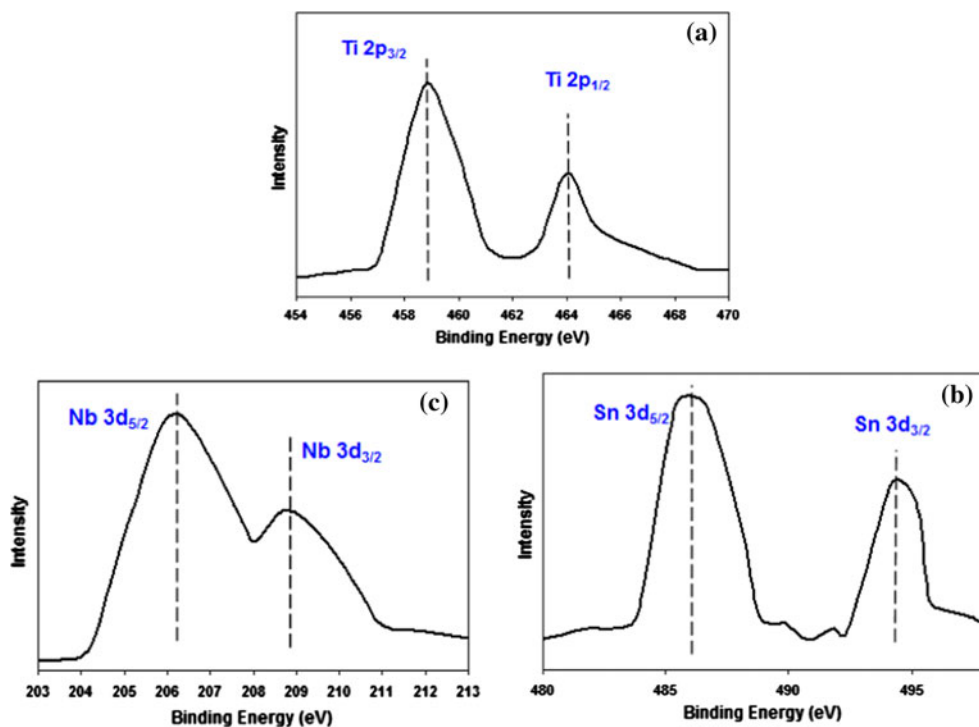
Also, the lattice parameters and cell volume of the TiO<sub>2</sub> and doped TiO<sub>2</sub> thin films are summarized in Table 1. It is obvious that the lattice parameters and cell volume of the doped TiO<sub>2</sub> thin films increase with increasing amount of Sn an Nb substitution for Ti<sup>4+</sup> in titania lattice.

### 3.2 XPS and BET analysis of the thin films

X-ray photoelectron spectroscopy is a highly sensitive technique of surface analysis, and is an effective method to investigate the surface composition and chemical states of solid samples. XPS measurements were carried out to determine the surface composition and chemical state of Sn or Nb doped TiO<sub>2</sub> thin film calcined at 475 °C. All the binding energies were referenced to the adventitious C1s peak at 284.6 eV.

The binding energy of Ti 2p<sub>3/2</sub> and Ti 2p<sub>1/2</sub> were observed at approximately 458.8 and 464.1 eV, respectively (Fig. 2a), indicating that the Ti element mainly existed as the chemical state of Ti<sup>4+</sup> [31]. XPS spectra of Sn 3d region are given in Fig. 2b. Two peaks corresponding to Sn 3d<sub>5/2</sub> and Sn 3d<sub>3/2</sub> are observed. The peak position corresponding to Sn 3d<sub>5/2</sub> is located between those of Sn 3d<sub>5/2</sub> in SnO<sub>2</sub> (486.5 eV) and Sn 3d<sub>5/2</sub> in metallic

**Fig. 2** XPS analysis of calcined doped TiO<sub>2</sub> thin film **a** Ti 2p, **b** Sn 3d, **c** Nb 3d



Sn (485.0 eV), which is ascribed to incorporated  $\text{Sn}^{4+}$  in the lattice of  $\text{TiO}_2$  [32].

Figure 2c shows the Nb 3d spectrum for the doped film exhibiting two peaks at 206.3 and 208.8 eV [33]. The peaks represent the  $3d_{5/2}$  and  $3d_{3/2}$  components, respectively, with a spin–orbit splitting of 2.5 eV. The center of the Nb  $3d_{3/2}$  peak corresponds to that of  $\text{Nb}^{5+}$  oxidation state.

The nitrogen adsorption–desorption isotherm at 77 K and the BJH pore size distribution of sample calcined at 475 °C are showed in Fig. 3. It can be observed that the samples (T-15 %Sn and T-1 %Nb) exhibit the classical shape of a type IV isotherm according to the IUPAC classification, typical for mesoporous solids [34]. The existence of the hysteresis loop in the isotherms is due to the capillary condensation of  $\text{N}_2$  gas occurring in the mesopores. The surface area and the mean pore diameter of Sn-doped  $\text{TiO}_2$  film calcined at 475 °C are 106.97  $\text{m}^2/\text{g}$  and 12.2 nm (Fig. 3a, b) respectively. Also the surface area and the mean pore diameter of Nb-doped  $\text{TiO}_2$  film calcined at 475 °C are 150.61  $\text{m}^2/\text{g}$  and 10.1 nm (Fig. 3c, d), respectively. Table 2 shows the results from surface area measurements of the different samples.

### 3.3 Photocatalytic evaluation

Figure 4 shows the UV–Vis spectra of the pure  $\text{TiO}_2$  and the doped  $\text{TiO}_2$  thin films deposited on glazed porcelain

substrates in the wavelength range of 250–600 nm. In this figure, the absorption edge of Sn-doped  $\text{TiO}_2$  thin films shifts towards longer wavelengths, whereas absorption edge of Nb-doped  $\text{TiO}_2$  thin films shifts towards shorter wavelengths. It indicates a decrease (Sn doping) or increase (Nb doping) in the energy band gap (inset in Fig. 4).

The energy band gap corresponds to the absorption limit and can be roughly evaluated by using following equation:

$$E_g = 1240/\lambda_{\text{edge}}(\text{eV}) \quad (5)$$

where  $\lambda_{\text{edge}}$  represents the absorption limit of the semiconductor.  $\lambda_{\text{edge}}$  can be extracted from the absorption spectrum by carrying out the first derivative of absorbance with respect to wavelength near the absorption edge and finding the point at which the derivative spectrum reaches its minimum value. This point is actually the reflection point of the absorption curve. The tangent line of the absorption curve at the reflection point intersects with the x-axis on which absorbance reaches 0 and indicates  $\lambda_{\text{edge}}$ .

Doping  $\text{Sn}^{4+}$  has been found to be located approaching and below the conduction band [8]. Therefore, the red shift of the absorption edge for the Sn-doped  $\text{TiO}_2$  should be the result of the electronic transition from the valance band to the doping energy level. On the other hand, according to the XRD results, doping with Sn had accelerated the transformation from anatase to rutile phase of  $\text{TiO}_2$ , and the rutile phase has a band gap smaller than that of anatase, so

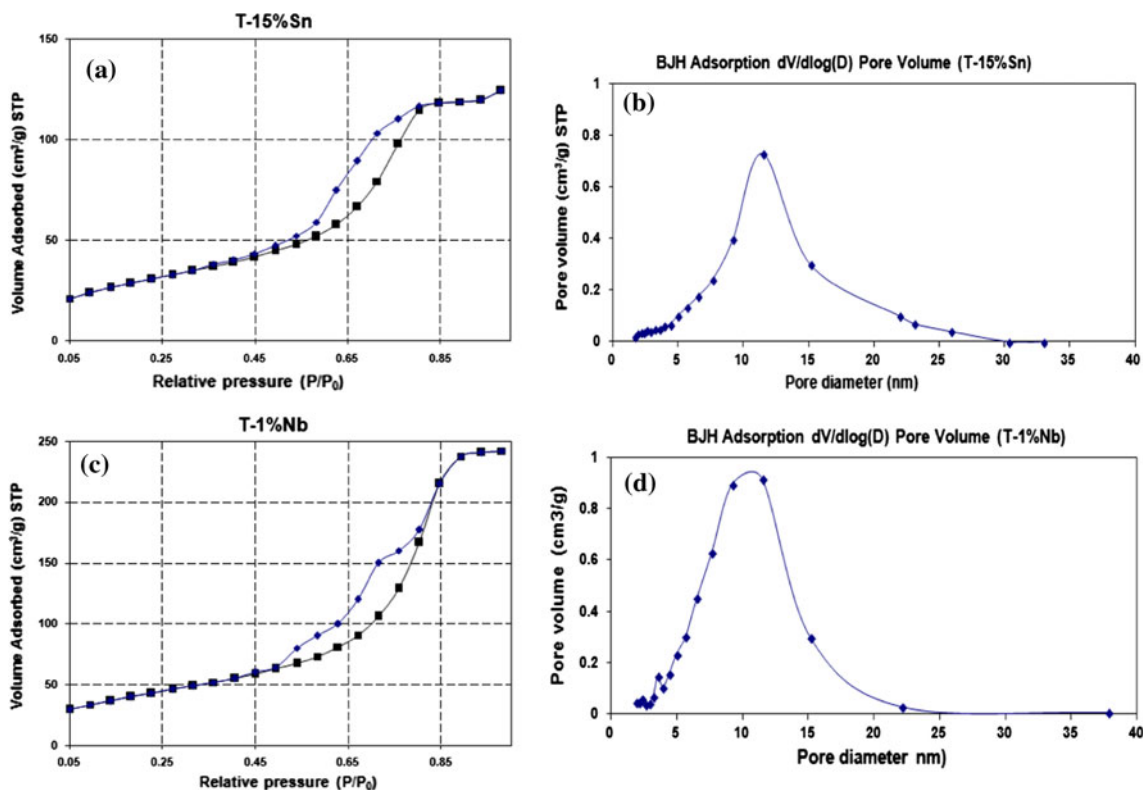


Fig. 3 Nitrogen adsorption–desorption isotherm a, b Sn-doped  $\text{TiO}_2$ . c, d Nb-doped  $\text{TiO}_2$

this transformation should be another reason for the red shift.

The band gap of the pure TiO<sub>2</sub> thin film was about 3.22 eV and had increased to 3.25 eV with increasing Nb content. The widening of the band gap can be explained by the Burstein–Moss (BM) effect [35], in which the lowest states in the conduction band were blocked, and transitions can take place only to energies higher than Fermi energy. Thus, the band gap became widened with increasing Nb content. The observed values were higher than the band gap of both bulk and thin film TiO<sub>2</sub> in the anatase phase. The reported values were 3.18 eV [36] for bulk material and in the range 3.2–3.23 eV for thin films [37].

Figure 5 shows the normalized concentration at 660 nm absorption of the MB solutions separated from the TiO<sub>2</sub> thin film as a photocatalyst under various time irradiations (0–120 min) to determine the photo-catalytic degradation: (1) under the UV irradiation and (2) under the visible light irradiation.

According to Fig. 5a, the order of photo-catalytic activity of TiO<sub>2</sub> thin films at 120 min under the UV irradiation was as following: T-1 %Nb > T-15 %Sn > T, but under the visible light irradiation (Fig. 5b), was T-15 %Sn > T-1 %Nb > T which suggests that the doping enhances the photo-catalytic activity of TiO<sub>2</sub> under both conditions. Non-doped Titania has lowest response in all irradiation ranges. T coatings have better response under UV light because of E<sub>g</sub> around 3.22 eV. This energy band is in UV light range. Near 76.2 % of MB was decomposed in the presence of T-1 %Nb film after UV irradiation for 120 min, while the values in the presence of T-15 %Sn and

T film are 42.4 and 36.4 %, respectively. Also, photo-catalytic activity of TiO<sub>2</sub> thin films at 120 min under the visible light irradiation obtained 83.68 and 33.88 and 21.08 % in the presence of T-15 %Sn, T-1 %Nb and T thin film, respectively.

Some studies indicated that the photo-catalytic activity of TiO<sub>2</sub> catalysts depends strongly on two factors: adsorption behavior and the separation efficiency of electron–hole pairs [38, 39]. On the one hand, the BET results showed that the specific surface areas of the catalysts increased from 85.93 m<sup>2</sup>/g for undoped TiO<sub>2</sub>–150.61 m<sup>2</sup>/g for Nb-doped TiO<sub>2</sub> and 106.97 m<sup>2</sup>/g for Sn-doped TiO<sub>2</sub>, significantly (shown in Table 2).

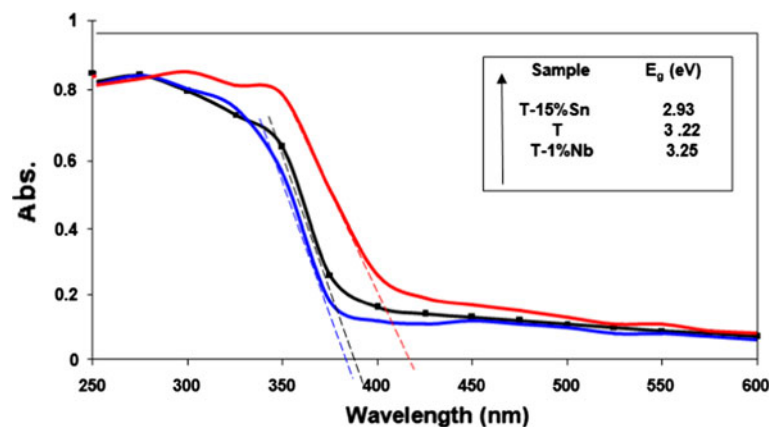
The larger specific surface area of doped TiO<sub>2</sub> catalysts would be beneficial to achieve better adsorption of MB in aqueous suspension. Therefore, the induce of dopant seems to be helpful for the photo-catalytic activity. According to Fig. 5 and Table 2, the photo-catalytic reactivity of doped TiO<sub>2</sub> thin film is higher than that of undoped TiO<sub>2</sub>, which is consistent with the larger specific surface area of doped TiO<sub>2</sub> than undoped TiO<sub>2</sub>.

The increase in photoactivity may be attributed to the combination of different processes: (1) decrease of the energy gap favoring higher photo excitation efficiency under solar radiation, and giving rise to a larger population of excited species (hole–electron pairs), (2) the small particles size favoring the increase in the surface per volume ratio, the scavenging action of photogenerated electrons by Sn<sup>4+</sup> or Nb<sup>5+</sup> ions thus preventing the recombination of electron–hole pairs and increasing the lifetime of charge carriers, so that they can take part in photo-catalytic processes, (3) the doping ions Sn<sup>4+</sup> or Nb<sup>5+</sup> can act as electron traps, thus facilitating the electron–hole separation and subsequent transfer of trapped electron to the adsorbed O<sub>2</sub> which acts as an electron acceptor on the surface of the TiO<sub>2</sub>, (4) the dopant contribute to prevent the recombination of electron–hole pairs, increasing the lifetime of charge carriers, so that they can take part in photo-catalytic processes. Based on Fig. 5a, under UV irradiation T-1 %Nb has larger

**Table 2** Surface area measurement of the different samples

Sample code	BET surface area (m <sup>2</sup> /g)
T (undoped)	85.93
T-1 %Nb	150.61
T-15 %Sn	106.97

**Fig. 4** UV–Vis absorption spectra of pure TiO<sub>2</sub> and doped thin films deposited on glazed porcelain substrate (calcined at 475 °C) with calculated energy band gaps of samples



decomposition ability than T-15 %Sn while T-15 %Sn has better decomposition ability under visible light irradiation. This can be caused by higher visible light absorbance of T-15 %Sn and higher UV light absorbance on T-1 %Nb.

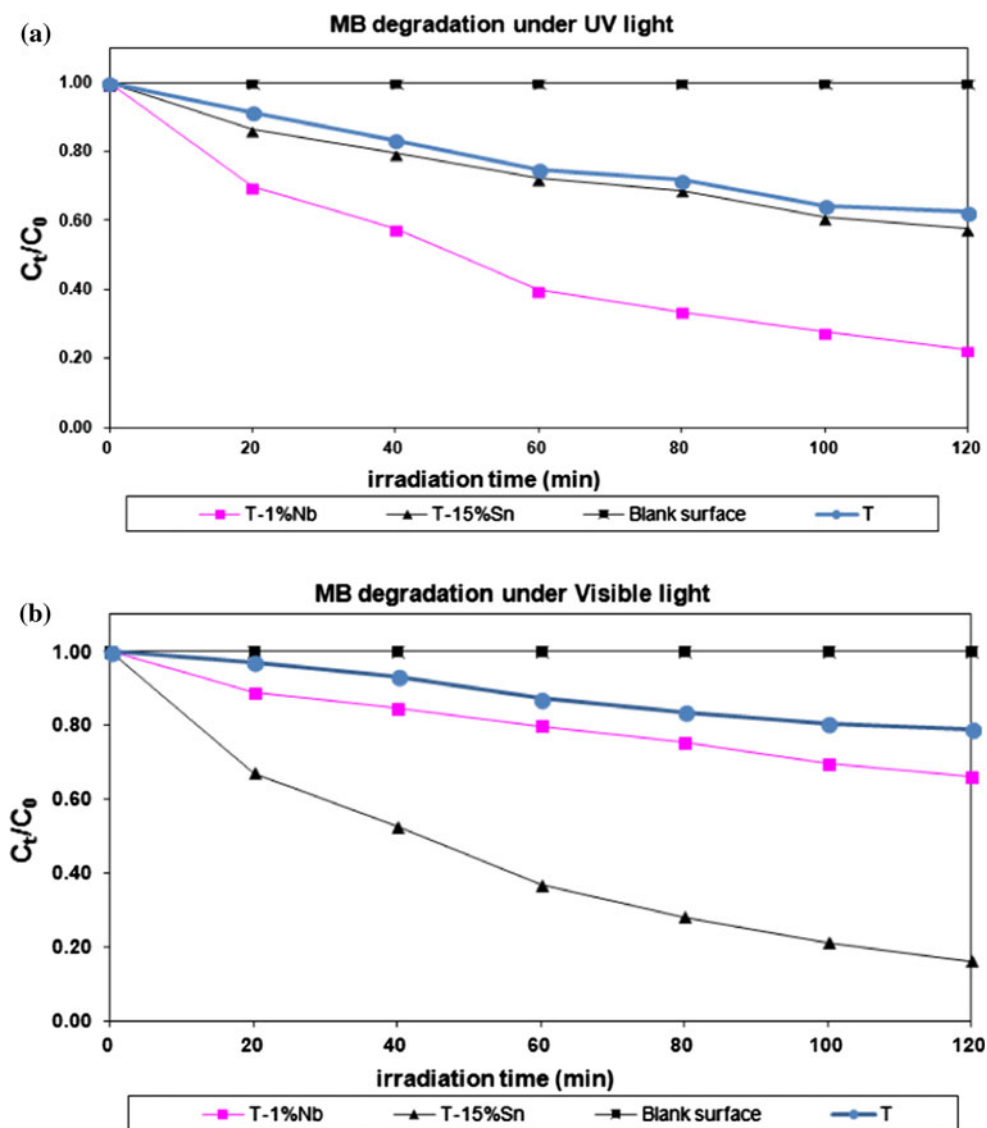
### 3.4 High resolution transmission electron microscopy (HR-TEM)

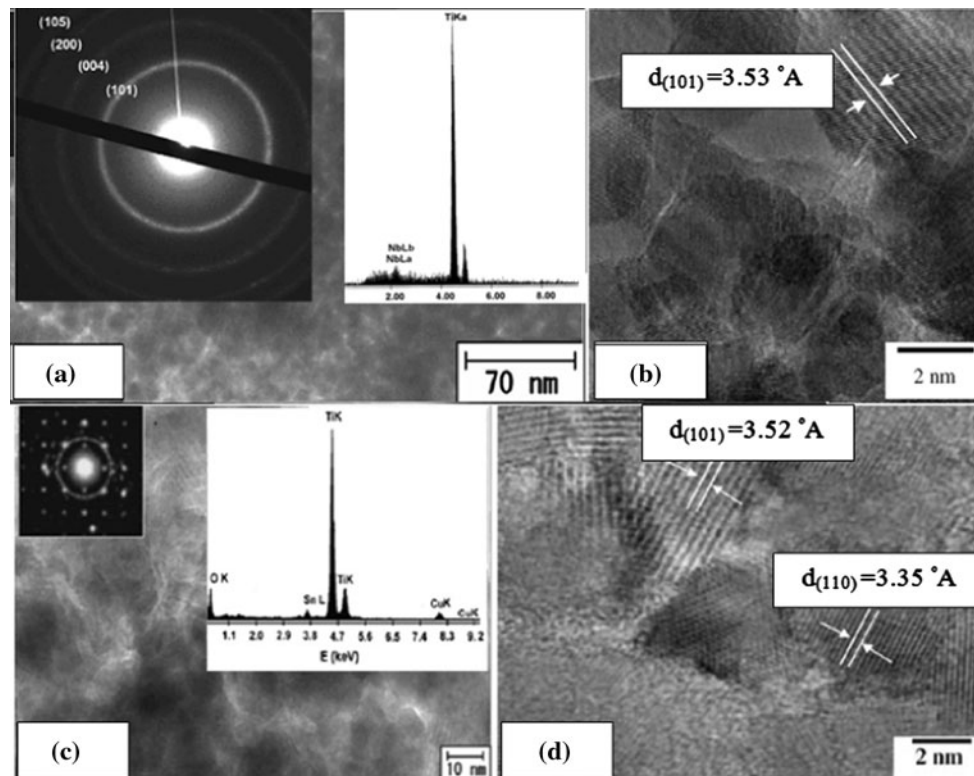
Figure 6 shows the surface of doped thin films (Fig. 6a, c). Surface was consisted of highly dense and uniform nanocrystalline  $\text{TiO}_2$ , with a porous structure and particle size around 10 nm. This figure also shows formation of crack-free thin film on glazed porcelain substrate. The thickness of the applied thin films on porcelain substrates was about 200 nm (not shown). The electron diffraction (ED) patterns of the selected area on Nb-doped  $\text{TiO}_2$  sample (inset of

Fig. 6a) shows the strong Debye–Scherrer rings indicating the anatase phase structure crystallite. Figure 6c shows the strong Debye–Scherrer rings and complicated bright spots, indicating the coexistence of polycrystalline anatase and rutile crystallites. This agrees with the aforementioned conclusion that the  $\text{Sn}^{4+}$  ions doped in  $\text{TiO}_2$  can promote the formation of rutile phase structure titania.

Figure 6b, d displays the HRTEM images of Nb-doped and Sn-doped  $\text{TiO}_2$  thin film, respectively. For anatase structure, the fringe spacing ( $d$ ) of (101) crystallographic plane is determined to be 3.50, 3.53 and 3.52 Å for undoped  $\text{TiO}_2$  film, T-1 %Nb and T-15 %Sn, respectively (Fig. 6b, d). This implies that  $\text{Sn}^{4+}$  ions are doped into  $\text{TiO}_2$  lattice in substitutional space in T-15 %Sn, since the ionic radius of  $\text{Sn}^{4+}$  (0.71 Å) is larger than that of the lattice  $\text{Ti}^{4+}$  (0.6 Å), a fringe spacing of 3.35 Å

**Fig. 5** Normalized concentration at 660 nm absorption of the MB solutions under various time irradiations, **a** under the UV irradiation, and **b** under the Visible light irradiation





**Fig. 6** TEM and HRTEM image of Nb-doped TiO<sub>2</sub> thin film (a, b) and Sn-doped TiO<sub>2</sub> (c, d)

corresponding to the (110) planes of rutile TiO<sub>2</sub> is observed in T-15 %Sn (Fig. 6d). All of these are consistent with the aforementioned XRD results.

The Sn and Nb ions are incorporated into the structure of titania coatings, which has been confirmed by SAED analysis. No rings corresponding of secondary phases, like SnO<sub>2</sub> or Nb<sub>2</sub>O<sub>5</sub>, were observed in SAED pattern for doped TiO<sub>2</sub> samples (Fig 6a, c -Top right).

The fringe spacing (*d*) of (101) crystallographic plane is 3.5 Å for undoped TiO<sub>2</sub> film [20] and is detected to be 3.53 and 3.52 Å for doped TiO<sub>2</sub>. This implies that Nb<sup>5+</sup> and Sn<sup>4+</sup> ions are doped into TiO<sub>2</sub> lattice in substitutional space in doped TiO<sub>2</sub>.

#### 4 Conclusion

In this research, Sn and Nb doped TiO<sub>2</sub> thin films with photo-catalytic properties have been prepared by a sol-gel dip-coating method. The anatase to rutile phase transformation was promoted by Sn<sup>4+</sup> doping but inhibited by Nb<sup>5+</sup> doping. The photo-catalytic activity of the doped thin film is higher than that of pure TiO<sub>2</sub> thin films. Sn<sup>4+</sup> and Nb<sup>5+</sup> substitution for Ti<sup>4+</sup> in the titania lattice results in a decrease in the rate of photogenerated electron-hole recombination that is responsible for the enhancement in

photo-catalytic degradation rate. Photo-catalytic activity of the doped thin film under UV and Visible irradiation was improved comparing to undoped TiO<sub>2</sub> thin films. Under UV irradiation T-1 %Nb has larger decomposition ability than T-15 %Sn while T-15 %Sn has better decomposition ability under visible light irradiation.

#### References

1. Yin S, Ihara K, Aita Y, Komatsu M, Sato T (2006) J Photochem Photobiol A Chem 179:105–114
2. Yin S, Yamaki H, Komatsu M, Zhang Q, Wang J, Tang Q (2003) J Mater Chem 13:2996–3001
3. Colon G, Hidalgo MC, Munuera G, Ferino I, Cutrufello MG, Navio JA (2006) Appl Catal B Environ 63:45–59
4. Li FB, Li XZ, Hou MF, Cheah KW, Choy WCH (2005) Appl Catal A Gen 285:181–189
5. Kubacka A, Fuerte A, Martinez-Arias A, Fernandez-Garcia M (2007) Appl Catal B Environ 74:26–33
6. Jin Z, Zhang X, Li Y, Li S, Lu G (2007) Catal Commun 8:1267–1273
7. Sayilkan HI (2007) Appl Catal A Gen 319:230–236
8. Xie Y, Yuan C (2004) Appl Surf Sci 221:17–24
9. Bouras P, Slathatos E, Lianos P (2007) Appl Catal B Environ 73:51–59
10. Kudo A (2007) Int J Hydrogen Energy 32:2673–2678
11. Cuiying H, Wansheng Y, Ligin D, Zhibin L, Zhengang S, Lancui Z (2006) Chin J Catal 27:203–209



12. Ihara T, Miyoshi M, Ando M, Sugihara S, Iriyama Y (2001) *J Mater Sci* 36:4201–4207
13. Ihara T, Miyoshi M, Iriyama Y, Matsumoto O, Sugihara S (2003) *Appl Catal B Environ* 42:403–409
14. Prokes SM, Gole JL, Chen X, Burda C, Carlos WE (2005) *Adv Funct Mater* 15:161–167
15. Litter MI (1999) *Appl Catal B* 23:89–114
16. Paola DA, GarciaLopez E, Ikeda S (2002) *Catal Today* 75:87–93
17. Peiia DA, Uphade BS, Smirniotis PG (2004) *J Catal* 221:421–431
18. Choi W, Termin A, Hoffmann MR (1994) *J Phys Chem* 98:13669–13679
19. Brezova V, Blazkova A, Karpinsky L (1997) *J Photochem Photobiol A-Chem* 109(2):177–183
20. Navio JA, Colon G, Litter MI (1998) *Appl Catal B* 16(2):187–196
21. Koozegar Kaleji B, Sarraf-Mamoory R, Nakata K, Fujishima A (2011) *J Sol-Gel Sci Technol* 60:99–107
22. Koozegar Kaleji B, Sarraf-Mamoory R, Fujishima A (2012) *Mater Chem Phys* 132:210–215
23. Baker RW (2004) *Membrane technology and application*. Wiley, Chichester
24. Sharma R, Bhatnagar M (1999) *Sens Actuators B* 56:215–219
25. Fresno F, Coronado JM, Tudela D, Soria J (2005) *Appl Catal B Environ* 55:159–167
26. Tai WP, Oh JH (2002) *Sens Actuators, B* 85:154–157
27. Kumar KN, Fray DJ, Nair J, Mizukami F, Okubo T (2007) *Scripta Mater* 57:771–774
28. Klug P, Alexander LE (1974) *X-Ray diffraction procedures*. Wiley, New York
29. Spurr RA, Myers H (1957) *Anal Chem* 29:760–762
30. Sayilkana F, Asiltürka M, Kirazb N (2009) *J Hazard Mater* 162:1309–1316
31. Sanjines R, Tang H, Berger H, Gozzo F, Margaritondo G (1994) *J Appl Phys* 75:2945–2951
32. Cao Y, Yang W, Zhang W, Liu G, Yue P (2004) *New J Chem* 28:218–222
33. Moulder JF, Stickle WF, Sool PE, Bomben KD (1992) *Handbook of X-ray photoelectron spectroscopy*. Perkin-Elmer, Eden Prairie
34. De Boer JH, Everett BH, Stone FS (1985) *Properties of porous materials*. Butterworths, London
35. Yang Y, Chen X, Feng Y, Yang G (2007) *Nano Lett* 7:3879–3883
36. Hu L, Yoko T, Kozuka H, Sakka S (1992) *Thin Solid Films* 219:18–23
37. Wang Z, Helmersson U, Käll PO (2002) *Thin Solid Films* 405:50–54
38. Fujishima A, Rato TN, Tryk DA (2000) *J. Photochem Photobiol C: Photochem Rev* 1:1–21
39. Kamat PV (1993) *Chem Rev* 93:267–300